

# Imaging of the microstructure of Carbopol dispersions and correlation with their macroelasticity: A micro- and macrorheological study

Claude Oelschlaeger, Jonas Marten, Florian Péridont, et al.

Citation: *Journal of Rheology* **66**, 749 (2022); doi: 10.1122/8.0000452

View online: <https://doi.org/10.1122/8.0000452>

View Table of Contents: <https://sor.scitation.org/toc/jor/66/4>

Published by the [The Society of Rheology](#)

---

## ARTICLES YOU MAY BE INTERESTED IN

[Rheology and microstructure of discontinuous shear thickening suspensions](#)

*Journal of Rheology* **66**, 731 (2022); <https://doi.org/10.1122/8.0000317>

[Transient dynamics of soft particle glasses in startup shear flow. Part II: Memory and aging](#)

*Journal of Rheology* **66**, 717 (2022); <https://doi.org/10.1122/8.0000448>

[Extensional rheology and flow-induced crystal alignment in polypropylene ionomers](#)

*Journal of Rheology* **66**, 657 (2022); <https://doi.org/10.1122/8.0000404>

[Understanding the complex rheology of human blood plasma](#)

*Journal of Rheology* **66**, 761 (2022); <https://doi.org/10.1122/8.0000442>

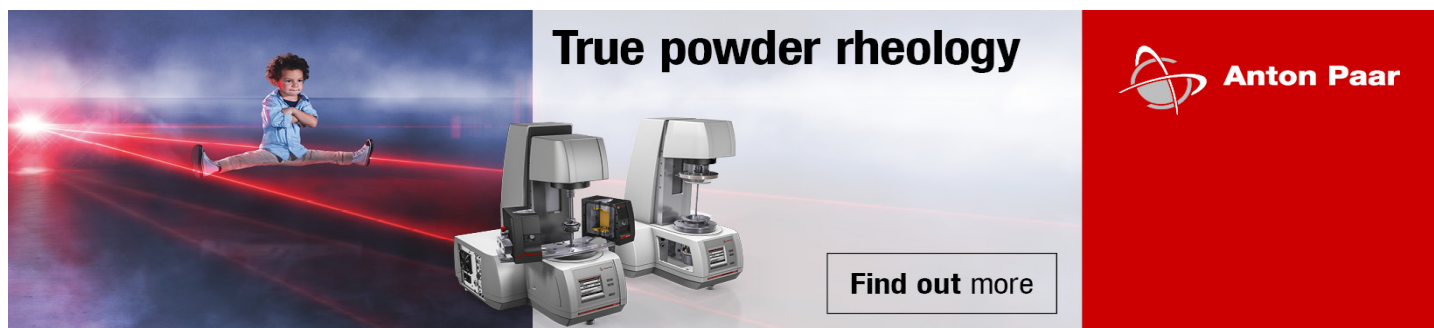
[On Oreology, the fracture and flow of “milk's favorite cookie<sup>®</sup>”](#)

*Physics of Fluids* **34**, 043107 (2022); <https://doi.org/10.1063/5.0085362>

[Rheology of \*Candida albicans\* fungal biofilms](#)

*Journal of Rheology* **66**, 683 (2022); <https://doi.org/10.1122/8.0000427>

---



The advertisement features a composite image. On the left, a young child in a blue shirt is performing a split leap on a dark surface, with red laser lines extending from their feet across the floor. In the center, two Anton Paar rheometers are shown. The text 'True powder rheology' is prominently displayed in the upper right. The Anton Paar logo and name are in the bottom right corner. A 'Find out more' button is located at the bottom center.

**True powder rheology**

**Anton Paar**

**Find out more**



# Imaging of the microstructure of Carbopol dispersions and correlation with their macroelasticity: A micro- and macrorheological study

Claude Oelschlaeger,<sup>a)</sup> Jonas Marten, Florian P ridont, and Norbert Willenbacher

*Institute of Mechanical Process Engineering and Mechanics, Applied Mechanics Group, Karlsruhe Institute of Technology, Karlsruhe, Germany*

(Received 7 February 2022; final revision received 18 May 2022; published 13 June 2022)

## Abstract

We developed a new data analysis strategy, the so-called micro-rheo-mapping technique, based on multiparticle tracking experiments to obtain an accurate and direct visualization of the microstructure of commercial acrylate thickeners of Carbopol-type with high (Ultrez 10), intermediate (ETD 2020), and low (ETD 2050) degree of crosslinking. At low polymer concentration, aggregates made of several primary Carbopol particles are formed with an average diameter of  $43 \pm 11$ ,  $56 \pm 14$ , and  $10 \pm 2.5 \mu\text{m}$  for Ultrez 10, ETD 2020, and ETD 2050, respectively. For ETD 2050, the least crosslinked thickener, the shell of dangling polymer chains covering the aggregate surface is thicker than for ETD 2020 and Ultrez 10. At technically relevant polymer concentrations, our results indicate, for all three thickeners, that the microstructure is highly heterogeneous with regions of different crosslink densities. One region inaccessible for tracer particles corresponding to a mixture of polydisperse aggregates and individual primary particles with a core mesh size less than 200 nm and a second, diluted enough to be accessible and which exhibits both elastic and viscous characteristics. The study of the impact of *pH*, polymer concentration, and crosslink density on these local structural and viscoelastic heterogeneities as well as macrorheological properties allowed us to establish a correlation between microstructure and macroelasticity. In particular, we found that the bulk shear modulus strongly depends on the fraction of inaccessible areas, making this microscopic parameter most relevant for describing the macroelasticity of Carbopol gels, whereas the local elasticity of the interstitial regions is of minor importance.   2022 Author(s). All article content, except where otherwise noted, is licensed under a Creative Commons Attribution (CC BY) license (<http://creativecommons.org/licenses/by/4.0/>). <https://doi.org/10.1122/8.0000452>

## I. INTRODUCTION

Carbopol materials are synthetic acrylic polymers widely used as thickening agents in many applications including water-based coatings, personal care, and pharmaceutical products [1] and references therein. It consists of high molecular weight polymers, made up of homopolymers of acrylic acid and copolymers of acrylic acid and long chain alkyl acrylate crosslinked with allyl ethers of polyalcohols. Carbopol has been the subject of a considerable number of publications over the past decades and continues to generate great interest in fundamental research to this day. Most studies mainly cover aspects related to the yield stress [2–8] and thixotropic properties [9–12]. Recent studies also focus on Carbopol mechanical and structural properties under confined microscopic flow conditions [13,14]. In this study, we focus on an aspect that from a technical point of view is of utmost importance, namely, the extraordinary thickening efficiency of these products in comparison to other commercial acrylic thickeners [15]. Figure 1 illustrates this phenomenon by representing the variation of the elastic plateau modulus  $G_0$  as a function of the polymer concentration for various commercial thickeners: three of Carbopol-type, namely, Ultrez 10, ETD 2020, and ETD 2050 (Lubrizol Advanced Materials, Cleveland, USA) and two

others produced by the BASF SE (Ludwigshafen, Germany): Viscalex HV30 and Sterocoll D. However, all thickeners are composed of similar main monomers, Carbopol dispersions exhibit a much higher elasticity than Sterocoll and Viscalex solutions, particularly, at a low polymer concentration.

At a polymer concentration of 0.2 wt. %,  $G_0$  values for Carbopols vary between 20 and 300 Pa, which is about two orders of magnitude higher than values obtained for Viscalex HV30 and Sterocoll D with  $G_0 = 1$  and 0.05 Pa, respectively. Similar results to  $G_0$  are obtained by measuring the yield stress as will be shown and discussed in the Experimental section. An explanation of this remarkable thickening efficiency of Carbopol dispersions has been provided by Kowalczyk *et al.* [15] based on multiparticle tracking (MPT) microrheological measurements.

The microstructure of a Carbopol ETD 2050 dispersion was shown to be highly heterogeneous, corresponding to fluctuations in polymer concentration, compared to the homogeneous Sterocoll D and Viscalex HV30 solutions. Obviously, the presence of these heterogeneities is responsible for the high thickening efficiency of Carbopol-type thickeners. These microheterogeneities were for the first time imaged using Voronoi diagrams. This representation allows for a direct mapping of the microstructure of the sample in terms of viscous and elastic regions, in other words, the microstructure of Carbopol has been imaged based on a “rheological contrast.” Many other studies report on the microstructure of Carbopol dispersions using different techniques

<sup>a)</sup> Author to whom correspondence should be addressed; electronic mail: [Claude.Oelschlaeger@kit.edu](mailto:Claude.Oelschlaeger@kit.edu)

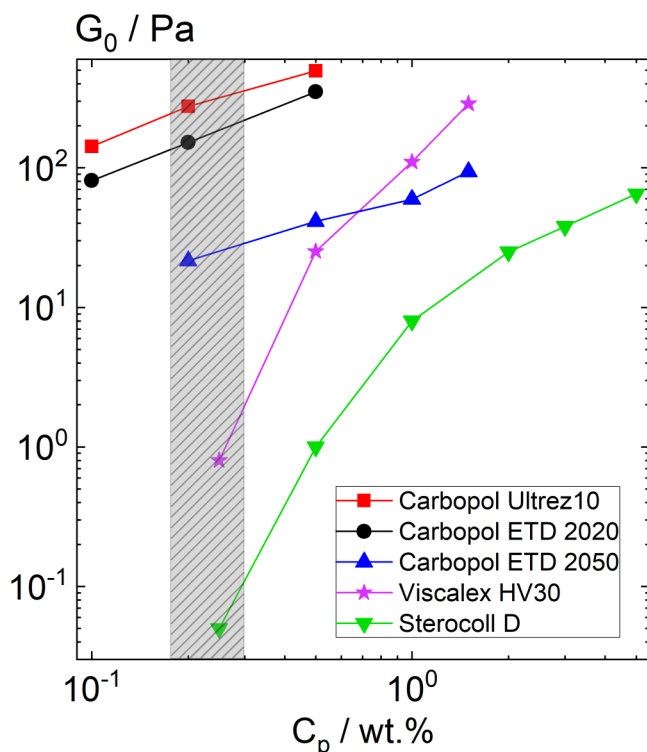


**FIG. 1.** Variation of the elastic plateau modulus  $G_0$  as a function of the polymer concentration  $C_p$  for Carbopol-type thickeners: Ultrez 10 (red), ETD 2020 (black), ETD 2050 (blue), and BASF-type thickeners: Viscalex HV30 (violet) and Sterocoll D (green).

such as fluorescence confocal microscopy [9,13,14,16–18], cryogenic scanning electron microscope (cryo-SEM) [18–20], static light scattering [19,21], laser diffraction [22,23], and even microrheology [2,3], but they only give partial information on the microstructure due, in particular, to the limited resolution and artefacts occurring using these techniques. However, from these literature reports, it is generally accepted that dry Carbopol particles are highly polydisperse with a diameter ranging between 0.2 and 6  $\mu\text{m}$  [1]. This result suggests that these particles are agglomerates of individual primary particles since the maximum size of a single, dry spherical Carbopol macromolecule has been estimated to be 0.41  $\mu\text{m}$  [24]. For hydrated as well as neutralized particles, this diameter can even be  $>10 \mu\text{m}$  depending on the stirring conditions [1,9,25]. In conclusion, independently of the state of the particle: dry, wet, or neutralized, Carbopol particles form agglomerates of several primary particles with a size well above 1  $\mu\text{m}$  depending on the stirring conditions. Nevertheless, more accurate characterization and visualization of the microstructure is still lacking, in particular, a better description of the distribution of the crosslink density within these microgels, and, above all, little is known so far about the evolution and contribution of these microscopic features on bulk viscoelastic properties. Therefore, in the present study, we developed a new microrheology method, namely, the so-called micro-rheo-mapping (MRM) technique in order to obtain an even more accurate characterization of the Carbopol microstructure with the aim of better understanding how local structural and micromechanical properties impact macromechanical properties.

In the first part of this paper, we describe in detail the new MRM data analyzing strategy based on the multiple particle tracking (MPT) microrheology experiments exemplarily applied to an aqueous solution of Carbopol Ultrez 10. Then, using this new approach and classical rotational rheometry, we investigate the impact of  $p\text{H}$ , polymer concentration, and crosslink density on both micro- and macrorheological properties of three types of Carbopol of different degrees of crosslinking, namely, Ultrez 10, ETD 2020, and ETD 2050, highly, moderately, and weakly crosslinked, respectively. Results will help us to establish a relationship between microscopic features and bulk viscoelastic properties aiming at a deeper insight into the thickening mechanism for each of the thickeners.

## II. EXPERIMENTAL

### A. Preparation of Carbopol dispersions

All acrylic thickeners, namely, Carbopol Ultrez 10 (CBP1098), Carbopol ETD 2020 (CBP1070A), and Carbopol ETD 2050 (CBP1071) were obtained from Lubrizol Advanced Materials Europe in powder form. The basic route for preparing Carbopol dispersions is to first dissolve the Carbopol powder by gently stirring it in de-ionized water, then to neutralize this acidic solution with the addition of the base sodium hydroxide NaOH, 4N (Carl Roth) [26].

For each type of Carbopol, the first step of sample preparation was to produce a stock solution of 2 wt. % of Carbopol dissolved in de-ionized water, which reduces the phase separation after long time storage (Lubrizol: technical data). This stock solution was prepared by slowly sifting the dry polymer into water with moderate agitating (500 rpm for 1 h) using a 5 cm diameter 3-blade propeller stirrer. After complete dissolution, the solution was stirred one more hour at 100 rpm for good homogenization and, finally, stirred for 12 h with a magnetic stirrer at approximately 50 rpm. Then samples with different polymer concentrations, i.e., 0.01, 0.1, 0.2, and 0.5 wt. %, were prepared by dilution from this stock solution, and subsequently, these solutions were neutralized adding dropwise, under constant stirring of 50 rpm, different amounts of NaOH producing samples of different  $p\text{H}$  varying between 2.5 and 12. Before the samples were tested, they were centrifuged at 2000 rpm for 10 min to remove air bubbles and then stored for 24 h at room temperature.

### B. Macrorheology: Rotational rheometry

Oscillatory shear measurements were performed using two rotational rheometers (Haake Mars II and RheoScope 1 both from Thermo Fischer Scientific) equipped with plate-plate (diameter 20 or 35 mm, gap 0.5 or 1 mm) or cone-plate (diameter 50 or 35 mm, cone-angle  $1^\circ$ ) measuring cells, depending on the heterogeneity and elasticity of the sample. For all concentrations, frequency sweeps, covering the frequency range from 0.1 to 100 rad/s, were performed at a stress amplitude sufficiently small to provide a linear material response. From these modulus curves, the elastic plateau modulus  $G_0$  was determined as the value of the storage

modulus  $G'$  at  $\omega = 1 \text{ rad s}^{-1}$  where it exhibits a constant plateau.

### C. Microrheology: Multiple particle tracking

A detailed scheme of the MPT setup used in this study is described in Kowalczyk *et al.* [15]. It is based on an inverted fluorescence widefield microscope (Axio Observer D1, Carl Zeiss) equipped with a Fluar 100 $\times$  objective (numerical aperture 1.3, 100 $\times$  magnification, oil immersion lens, Carl Zeiss). Green fluorescent carboxylate-modified polystyrene microspheres of 0.1, 0.2, and 0.5  $\mu\text{m}$  diameter with a density of 1.06 g/cm<sup>3</sup> and a refractive index of 1.59 at 589 nm were used as tracer particles (Bangs Laboratories, USA). To ensure no specific interactions between these tracer particles and the polymer, we also performed experiments using non-functionalized polystyrene particles as well as sterically stabilized polyethylene glycol-grafted polystyrene particles and in all cases, similar results were obtained. Carbopol dispersion ( $\sim 20 \mu\text{l}$ ) including the tracer particles was injected into a self-build closed chamber consisting of a coverslip and microscope glass slide (width 2 mm, length 10 mm, and thickness 0.15 mm) sealed with a UV-curing optical adhesive. The microscope was focused roughly halfway into the sample, i.e., at a distance of 20–40  $\mu\text{m}$  away from the surface, to minimize wall effects. 2D images (field of view 127  $\times$  127  $\mu\text{m}$ , frame rate 50 frames/s) of the fluorescent particles were recorded using an sCMOS camera Zyla X (Andor Technology). Movies of the fluctuating microspheres were analyzed by a custom MPT routine incorporated into the software Image Processing System (Visiometrics iPS) [27,28]. Particle tracking and calculation of MSD, as well as the statistical analysis of the trajectories was done using a self-written MATLAB<sup>®</sup> program [15] based on the widely used Crocker and Grier tracking algorithm [29]. Tracer particles were added before neutralization with NaOH, i.e., prior to gelation, to ensure the homogeneous distribution of the tracer particles within the sample.

## III. RESULTS AND DISCUSSION

### A. MRM technique for accurate characterization of the Carbopol microstructure

As mentioned previously, this new MRM technique has been developed for accurate characterization and visualization of the Carbopol microstructure. MRM combines Voronoi triangulation results obtained from a conventional MPT analysis discarding short particle trajectories with the image overlay technique including all trajectories generated during a tracking experiment. The different steps of this new approach, applied to a Carbopol Ultrez 10 solution, are described in Sec. III A 1-3.

#### 1. Image overlay

For the image overlay technique, the result is simply the superposition of all particle trajectories across all images of the video sequence. Figure 2(a) shows the overlay of 500 images for a neutralized ( $\text{pH} = 11$ ) 0.5 wt. % Carbopol Ultrez solution obtained tracking polystyrene microspheres of diameter 0.2  $\mu\text{m}$ . All trajectories ( $\approx 80\,000$ ), in black, do not cover

the whole sample, leading to the visualization of large white areas where no tracer particles were present during the whole measurement. These white areas correspond to a mixture of aggregates and individual primary particles, inaccessible for the diffusing 200 nm tracer particles.

The black areas correspond to regions dilute enough to be accessible for the particles and these areas have been analyzed using MPT in a conventional way by discarding all short trajectories composed of less than 15 frames. In this case, a total number of  $\approx 1000$  trajectories is left from which the classical Voronoi diagrams are constructed as described in Sec. III A 2. It should also be mentioned here that Fig. 2(b) is obtained by simply inverting the colors of Fig. 2(a) with now, the inaccessible regions shown in black.

#### 2. Voronoi diagram

The 1000 trajectories obtained after discarding all short trajectories are transformed into mean square displacement (MSD) traces [30] and their dependence on lag time  $\tau$  is displayed in Fig. 2(c). A broad variation in absolute values and time dependence of the individual MSDs is found. This result clearly reveals a heterogeneous structure on the micrometer length scale and is confirmed by the statistical analysis of the MSD distributions via van Hove diagrams with a non-Gaussian parameter  $\alpha = 5.7$  [31]. For an ergodic homogeneous system, the distribution of MSD values at any instant of time should be Gaussian corresponding to  $\alpha = 0$ . This ensemble of MSDs is then arbitrarily divided into two MSD populations with slopes  $\beta < 0.5$  and  $\beta > 0.5$  at a certain lag time. MSDs with  $\beta < 0.5$ , which account for 63% of the total MSDs, correspond to small time-independent particle displacement within highly elastic regions, whereas  $\beta > 0.5$  (27% of the total MSDs) characterizes larger particle displacements within viscous regions. This simplification leads to the determination of apparent values of the elastic modulus and viscosity as described below. From the averaged MSD of all MSDs  $> 0.5$  and using the relation  $\langle \Delta \bar{r}^2(\tau) \rangle = 4D\tau$  with  $D = k_B T / 6\pi\eta a$ , the local apparent viscosity  $\eta_{MPT}$  within viscous areas can be determined and was found to be 9.4 mPa s. Here,  $a$  stands for the radius of the embedded beads,  $k_B$  for the Boltzmann constant, and  $T$  for the temperature. Additionally, from the averaged MSD of all MSDs  $< 0.5$  and using the relation  $G_0 = \frac{2k_B T}{3\pi a \langle \Delta r^2(\tau) \rangle}$  [32], the local apparent elasticity within the elastic areas has been determined to be  $G_{0,MPT} = 2.4 \text{ Pa}$ . The size and spatial distribution of heterogeneities can be visualized using Voronoi diagrams [33] [Fig. 2(d)]. This representation allows for a direct mapping of the microstructure of the sample in terms of viscous (blue) and elastic (red) regions corresponding to the spatial distribution of polygons around particles with slopes of the MSD traces  $\beta > 0.5$  (viscous) and  $\beta < 0.5$  (elastic), respectively [15]. As will be discussed later, the reason for this local elasticity is most likely due to the overlapping of free polymer chains covering the highly dense core of an individual Carbopol particle, and which form an entanglement network when aggregates or particles come into contact. Indeed, based on our MRM results [Fig. 3(a)], we can exclude that a confinement effect of the tracer

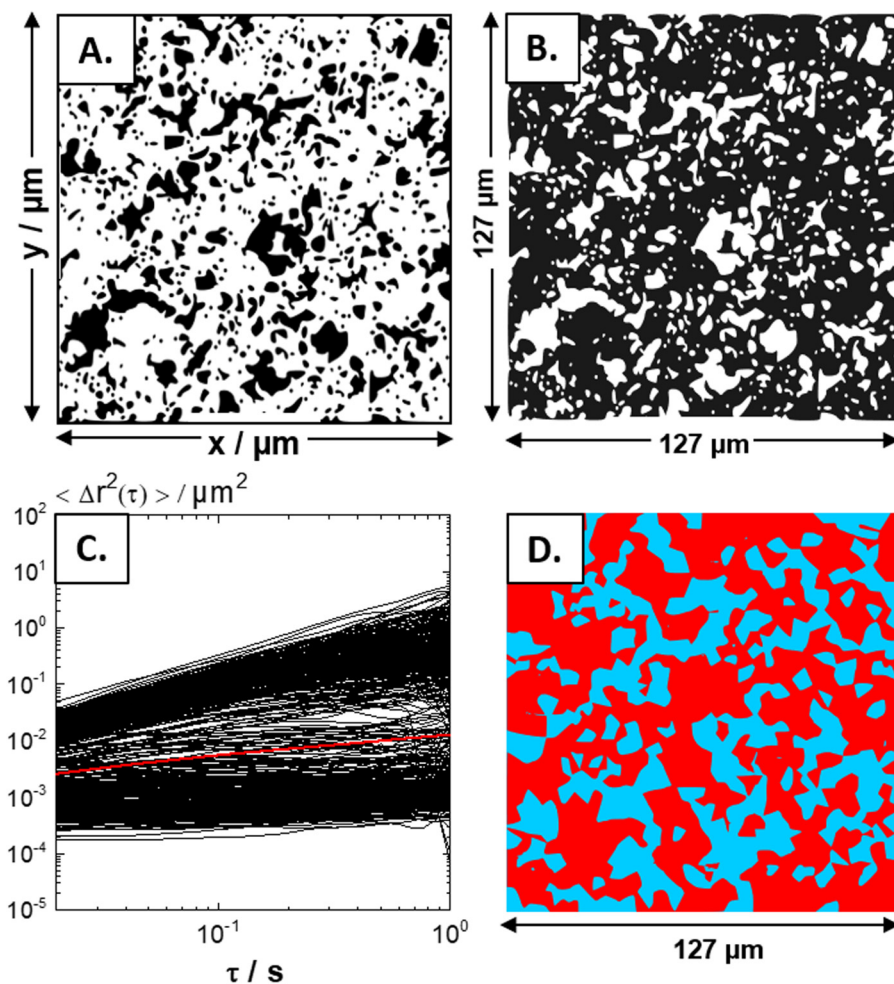


**FIG. 2.** (a). Overlay image containing all trajectories ( $\approx 80\,000$ ) (black lines). White areas correspond to the region inaccessible for the tracer particles. (b) Inversion of the colors of (a). (c) MSD plots corresponding to trajectories of minimum 15 frames. (d) Corresponding Voronoi diagram: viscous and elastic areas are in blue and red, respectively.

particles is the origin of this elasticity because the average size of both elastic and viscous areas accessible for the tracers is much larger than the diameter of an individual tracer particle, i.e.,  $0.2 \mu\text{m}$ .

### 3. Micro-Rheo-Mapping

Finally, by superimposing Figs. 2(b) and 2(d), we obtained an accurate and direct visualization of the heterogeneous microstructure of the polymer thickener based on a

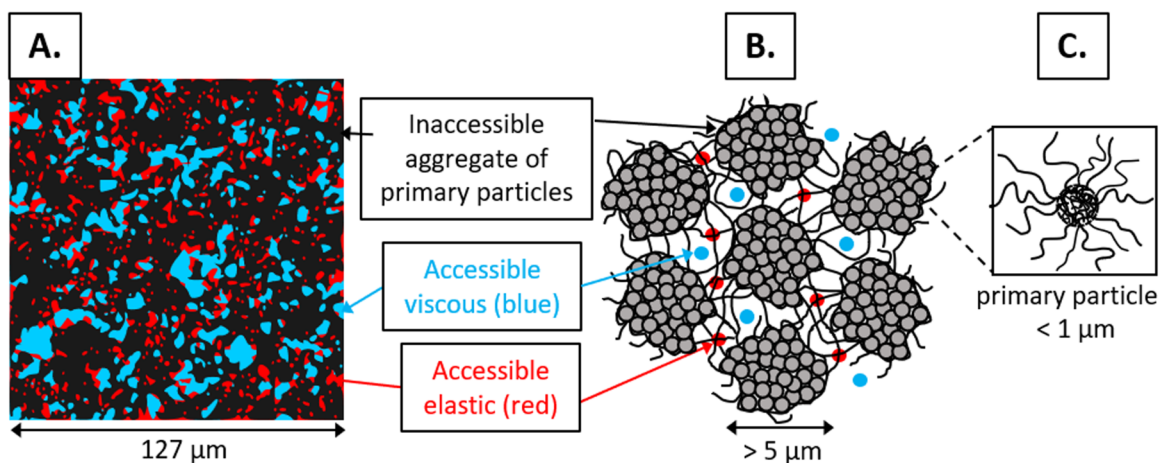


**FIG. 3.** (a). Micro-rheo-mapping: Voronoi diagram combined with an overlay image for a Carboxypol Ultrez 10 polymer thickener after neutralization. Viscous (blue) and elastic (red) accessible areas for tracer particles obtained from the Voronoi diagram. The black areas, obtained from the overlay technique, correspond to a mixture of aggregates of primary particles and individual primary particles, inaccessible for the tracer particles. (b). Schematic drawing representing the Carboxypol microstructure. (c) Primary particle with its highly crosslinked core and dangling ends.

“rheological contrast” as shown in Fig. 3(a). The black areas correspond to a mixture of polydisperse agglomerates of primary particles strongly bond together and individual primary particles inaccessible to the tracer particles. It represents  $\sim 70\%$  of the total area. The red ( $\sim 13\%$ ) and blue ( $\sim 17\%$ ) areas correspond to elastic and viscous regions, respectively, where tracer particles are able to diffuse into the structure. The validity of this new analyzing procedure has been confirmed by superimposing the raw video sequence including the fluorescent tracer particles with the resulting MRM mapping, as can be seen in Fig. 4 (Multimedia view). The result shows a perfect matching between the three regions determined on the MRM map with those directly observed on the video, namely, regions without tracer particles, regions where particles move freely, and others where their mobility is very restricted. Finally, an illustration, deduced from this MRM mapping, representing the Carbopol Ultrez 10 microstructure can be made and is shown in Figs. 3(b) and 3(c).

In summary, this new MRM approach combining the overlay image and Voronoi diagram is a powerful and versatile tool for obtaining accurate information about microstructural and micromechanical properties of heterogeneous materials such as Carbopol heterogeneous thickeners. In particular, the distribution, the average size, and area fractions of the different regions, as well as local values of the apparent plateau modulus  $G_{0,MPT}$  and apparent viscosity  $\eta_{MPT}$  can be determined. Using this new approach, in combination with rotational rheometry will allow us to study the impact of  $pH$ , polymer concentration, and crosslink density on both micro- and macrorheological properties of different types of Carbopol. Results will help us to understand how these microscopic features are related to macroscopic flow properties and shed light on the highly efficient thickening mechanism present in these polymers.

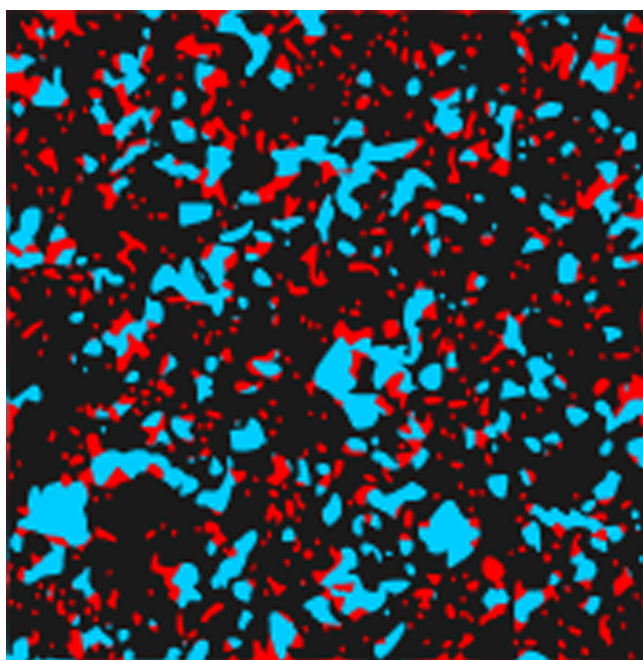


FIG. 4. Video sequence confirming the validity of the new MRM analyzing procedure. Multimedia view: <https://doi.org/10.1122/8.0000452.1>

## B. MPT microrheology at a low polymer concentration of 0.01 wt. %

### 1. Structural characterization of Carbopol aggregate and primary particle

Prior to characterizing the microstructure of concentrated Carbopol solutions at technically relevant polymer concentrations suitable for efficient thickening, we investigated the structural properties of diluted systems at a very low polymer concentration of 0.01 wt. %, both before and after neutralization ( $pH \approx 5$ ) for each type of Carbopol. The goal is to characterize the size and swelling behavior of individual aggregates of primary Carbopol particles which, even after neutralization, do not interpenetrate to form an elastic percolated network. We performed MPT measurements using tracer particles of diameter  $0.2 \mu\text{m}$  and by means of the image overlay technique, we characterize the size of these aggregates which corresponds to the size of the areas inaccessible to the tracer particles. An example of the overlay image obtained for a 0.01 wt. % neutralized Carbopol ETD 2020 dispersion is shown in Fig. 5(a) with black and white areas representing accessible and inaccessible regions for the tracer particles, respectively. Similar results, but less well defined due to the spatial resolution limitation of our setup, were obtained using  $0.1 \mu\text{m}$  tracer particles indicating that the interactions between the primary particles are so strong that no tracer particles can penetrate into this structure but also that the mesh size of the dense core of each primary particle is clearly less than  $100 \text{ nm}$ .

Figure 5(b) represents the histogram of the size distribution of aggregates, corresponding to the cross-sectional area expressed in  $\mu\text{m}^2$ , before (filled, 22 counts) and after (open, 14 counts) neutralization, namely, in the unswollen and swollen states, respectively. In the unswollen state, the size of cross-sectional areas ranges from  $250$  up to almost  $7000 \mu\text{m}^2$  with a majority below  $1500 \mu\text{m}^2$ , resulting in an average size of approximately  $1460 \mu\text{m}^2$ . In the swollen state, the average size of the areas increases to  $2490 \mu\text{m}^2$ , which corresponds to an increase by a factor of 1.7. Under the assumption of perfectly round spheres, the diameter of the unswollen aggregates is approximately  $44 \pm 11 \mu\text{m}$  and that of the swollen ones  $56 \pm 14 \mu\text{m}$ . Thus, the diameter increases by  $\approx 30\%$ . It should be noted that these sizes are much larger than the diameter of a primary Carbopol particle, estimated to be  $\approx 0.2 \mu\text{m}$  by the manufacturer [34,35] but in the same range, between one and a few tens of micrometers, as has been found in other studies [17–19,21,36,37]. These measurements, therefore, confirm that the structures observed here are agglomerates consisting of several primary Carbopol particles. Table I summarizes the results obtained for all types of Carbopol differing in their degree of crosslinking.

First, we observe a decrease in the swelling ratio (SR) with increasing crosslink density, in agreement with theoretical literature statements [38].  $SR = 2.3$ ,  $1.7$ , and  $1.4$  for Carbopol ETD 2050, ETD 2020, and Ultrez 10, respectively. It should also be noted that these SR values are much lower than those generally found in the literature, namely,  $SR > 10$ . This is due to the fact that here the swelling behavior between the hydrated and neutralized state was determined

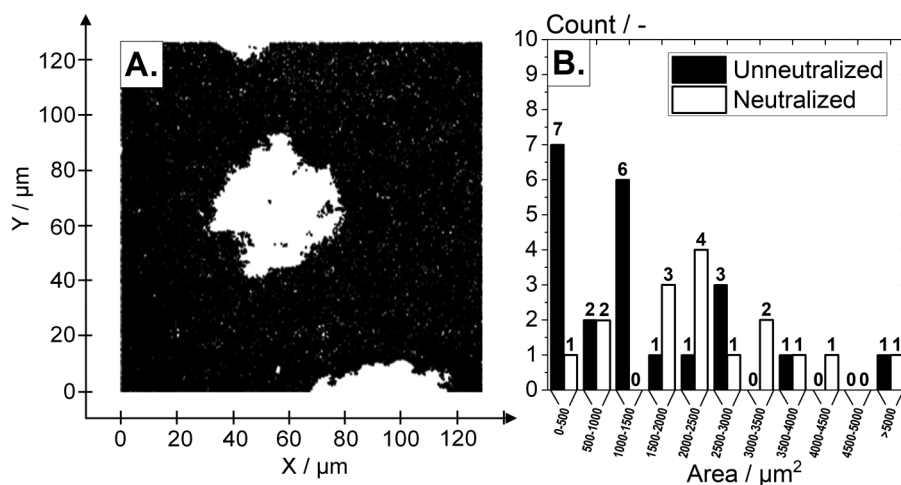


**FIG. 5.** (a). Overlay image for Carbopol ETD 2020 after neutralization at a polymer concentration of 0.01 wt. %. Black lines represent all trajectories. White areas correspond to region inaccessible for the 0.2 μm tracer particles. (b) Histogram of the size distribution of aggregates before (filled) and after (open) neutralization obtained for >14 aggregates.

for an agglomerate of particles and not for an individual Carbopol particle between the dried and neutralized state. There are also notable differences between the diameter of the individual aggregates of the various Carbopols both before and after neutralization. For example, in the neutralized regime, for both Ultrez 10 and ETD 2020 dispersions, aggregates diameters are  $43 \pm 11$  and  $56 \pm 14$  μm, respectively. These values are much higher than the diameter obtained for ETD 2050, which is only  $10 \pm 2.5$  μm. Another important structural difference between Carbopol ETD 2050 and the two other thickeners is deduced from MPT measurements performed with larger tracer particles of diameter 0.5 μm in the not neutralized regime at a higher polymer concentration of 0.5 wt. % when aggregates can come into contact. For both ETD 2020 and Ultrez 10 [Figs. 6(b) and 6(c), respectively], no accessible elastic areas, between aggregates, have been detected, while for ETD 2050, this is the case as indicated by the red areas in Fig. 6(a). This may be related to the number and length of the dangling polymer chains covering the surface of a primary particle and thus the surface of the agglomerates. Our results suggest that the number and length of these dangling chains in the case of ETD 2050 is much greater than for ETD 2020 and Ultrez 10. Indeed, for ETD 2050, when aggregates come into contact, even in the not neutralized regime, tracer particles can be trapped in an elastic network presumably formed by entangled long chains surrounding the surface of these agglomerates. We assume this is because ETD 2050 is the least crosslinked thickener in the series investigated here,

with a lower particle core density and, therefore, more polymer available for free dangling chains.

All these structural differences in aggregates and primary particles are illustrated in Fig. 7 and may affect the thickening mechanism and efficiency as discussed in Sec. III C.

### C. Micro- and macrorheological measurements at technically relevant polymer concentrations

In this section, results are obtained from measurements performed on Carbopol dispersions at technically relevant polymer concentrations of 0.5, 0.2, and 0.1 wt. %. The objective was to vary the bulk elasticity  $G_0$  of the three types of Carbopol in different ways and to establish a relationship between microstructure and macroelasticity to get a deeper insight into their thickening mechanism. To do this,  $G_0$  was modulated by varying the pH, polymer concentration, and degree of crosslinking, and at the same time, MRM experiments were performed to characterize microstructural changes. Results obtained are presented in Sec. III C 1 and the correlation between microstructure and macroelasticity is discussed in Sec. III C 2.

#### 1. pH, polymer concentration, and crosslink density effects on microstructure and elastic plateau modulus $G_0$

Figures 8(a)(1)–8(c)(1) show the effects of pH, polymer concentration, and crosslink density, respectively, on Carbopol macrorheological properties, namely, on the elastic plateau modulus  $G_0$ . In Figs. 8(a)(1) and 8(b)(1), only results obtained for Ultrez 10 are presented. Similar variations of  $G_0$  were obtained for Carbopol ETD 2020 and ETD 2050. The only difference resides in the absolute values of  $G_0$  which decrease according to the sequence Ultrez 10, ETD 2020, and ETD 2050. These data are shown in Fig. S1 in the [supplementary material](#) [43].

*a. pH effect.* For Ultrez 10 at a constant polymer concentration of 0.5 wt. % [Fig. 8(a)(1)], we observe that  $G_0$

**TABLE I.** Size and swelling behavior of an individual aggregate of Carbopol particles. Averaged over >10 measurements.

	ETD 2050	ETD 2020	Ultrez 10
Crosslink density	Low	Moderate	High
Swelling ratio (average areas)	2.3	1.7	1.4
Average aggregate diameter $d_p$	$10 \pm 2.5$	$56 \pm 14$	$43 \pm 11$
(swollen)/μm $d_p$ (unswollen)/μm	$6 \pm 1.5$	$44 \pm 11$	$36 \pm 9$

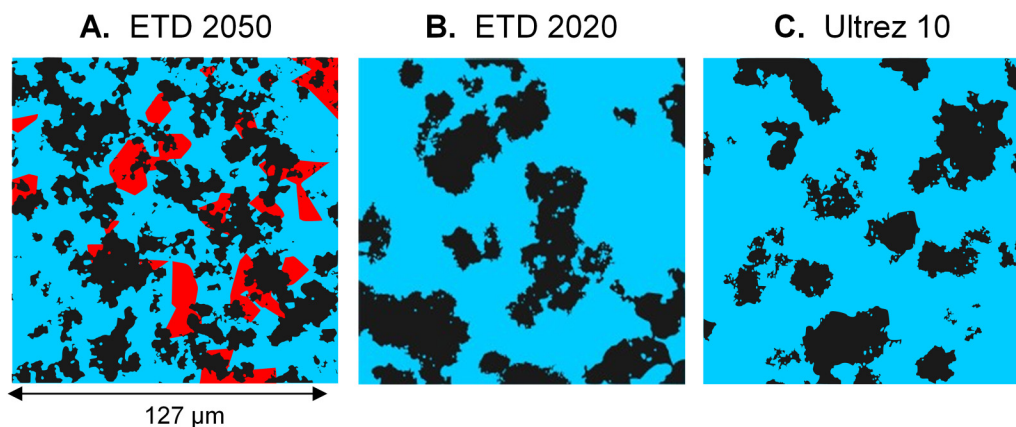


**FIG. 6.** MRM of not neutralized 0.5 wt. % ETD 2050 (a), ETD 2020 (b), and Ultrez 10 (c) dispersions. Black, blue, and red areas correspond to aggregates of primary particles inaccessible regions for the tracers, viscous, and elastic accessible regions, respectively.

significantly increases at low  $pH$ , reaches a maximum at intermediate  $pH$ , and then slightly decreases at higher  $pH$ . At low  $pH$  around 3, corresponding to the not neutralized regime, the dispersion exhibits a relatively low elasticity with  $G_0 \approx 2$  Pa. Then, increasing the  $pH$  leads to a drastic increase of  $G_0$  until it reaches a maximum ( $G_0 \approx 500$  Pa) at approximately  $pH$  5. After the maximum at  $pH > 5$ ,  $G_0$  decreases again but very slowly up to  $pH$  12 without ever reaching its initial value.

In summary, we conclude that the  $pH$  has a very strong impact on the macroelasticity of Carbopol. This is in accordance with previous studies [16,20] concerning the variation of another macroelastic parameter, namely, the yield stress  $\tau_y$ . This quantity was also determined here from rheological controlled-stress tests and its variation with  $pH$  is similar to that of  $G_0$  as shown (Fig. S2 in the [supplementary material](#)) [43]. Generally, this strong increase in elasticity with  $pH$  is explained by the formation of a sample spanning network but there is no clear evidence of what the microstructure is and how it changes upon variation of  $pH$ .

To fulfill this lack of knowledge, we performed micro-rheological experiments using the MRM technique in three relevant  $pH$  regimes: low (regime 1,  $pH \approx 3$ ), intermediate (regime 2,  $pH \approx 5$ ), and high (regime 3,  $pH \approx 12$ ) as indicated by the arrows in Fig. 8(a)(1). Regime 1 corresponds to

not neutralized samples of very low elasticity, regime 2 to neutralized samples with maximum elasticity, and regime 3 to samples with intermediate elasticity at  $pH$  well beyond the maximum. Results of MRM experiments performed on Ultrez 10 in these three regions of different  $pH$  are shown in Figs. 9(a)(1)–9(a)(3).

At first, we clearly see a modification of the Carbopol microstructure with increasing  $pH$  with a significant change in the distribution of the three microscopic areas, namely, of the inaccessible (black), accessible elastic (red), and accessible viscous (blue) areas as summarized in Fig. 9(a)(4). At low  $pH$  in the not neutralized regime (regime 1), only accessible viscous (blue) and inaccessible (black) areas are obtained, covering  $59 \pm 9\%$  and  $41 \pm 9\%$  of the total area of the image, respectively. A similar result is obtained for ETD 2020, while for ETD 2050 some elastic areas are present, as already discussed in Sec. III B 1 [Fig. 6(a)]. At intermediate  $pH$  (regime 2), the inaccessible area (black) covers  $87 \pm 3\%$  of the total area, the accessible elastic (red) and viscous (blue) areas  $8 \pm 3\%$  and  $5 \pm 1\%$ , respectively. Increasing the  $pH$  even further (regime 3), the fraction of inaccessible areas decreases again and reaches  $70 \pm 3\%$ . At the same time, the accessible elastic (red) and viscous (blue) areas increase to  $13 \pm 3\%$  and  $17 \pm 3\%$ , respectively. In addition to the change in the areas of distribution with  $pH$ , the analysis of the

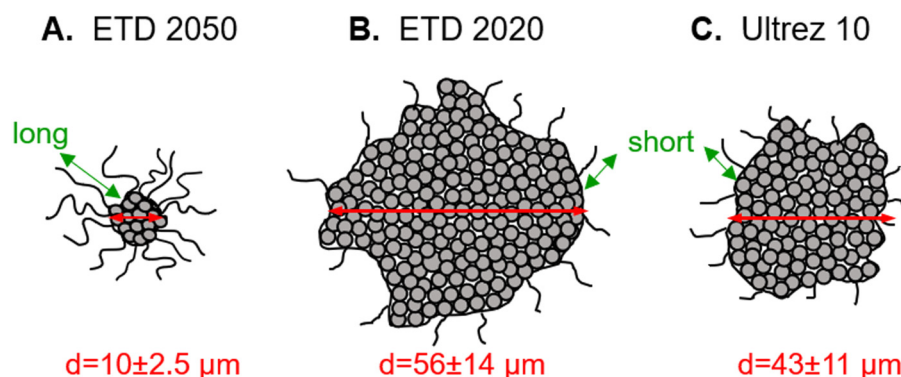


**FIG. 7.** Illustrations of an aggregate made of several primary Carbopol particles for neutralized ETD 2050 (a), ETD 2020 (b), and Ultrez 10 (c) as deduced from MPT measurements. Aggregate diameter (red line) and length of the dangling polymer chains (green line) covering the surface.



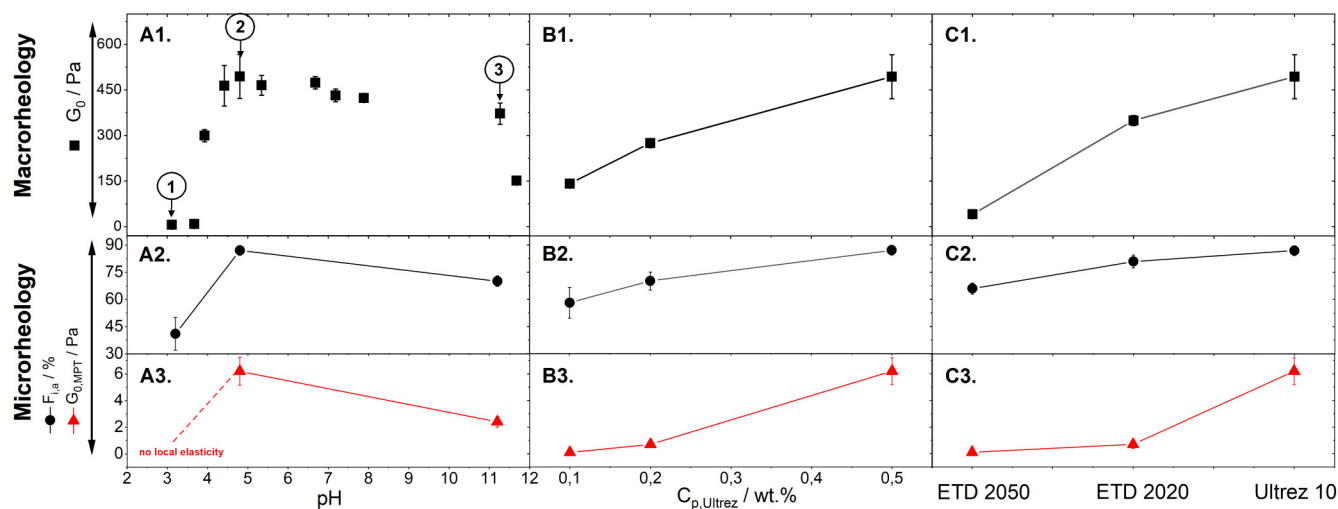


**FIG. 8.** Variations of the elastic plateau modulus  $G_0$ , fraction of the inaccessible area  $F_{i,a}$ , and local apparent elastic modulus  $G_{0,MPT}$  as a function of  $pH$  for an Ultrez 10 dispersion at a constant polymer concentration of 0.5 wt. % (a1)–(a3), as a function of the Ultrez 10 polymer concentration  $C_{p,Ultrez}$  (at intermediate  $pH$  corresponding to the maximum of elasticity) (b1)–(b3), and as a function of Carbopol type differing in their degree of crosslinking at a polymer concentration of 0.5 wt. % and intermediate  $pH$  (c1)–(c3).

average size of both accessible elastic (red) and viscous (blue) areas shows an increase in the size of these two regions when passing from regime 2 to 3, i.e., from the intermediate to the high  $pH$  regime (see Fig. S3(a) in the [supplementary material](#)) [43]. In regime 2, elastic and viscous regions have an average area size of  $\approx 1$  and  $\approx 3 \mu m^2$ , respectively, whereas in regime 3, it increases to  $\approx 2.6$  and  $\approx 10 \mu m^2$ , respectively.

These microstructural as well as bulk elasticity changes with increasing  $pH$  can be explained as follows. In the not neutralized regime at low  $pH$  [Fig. 9(a)(1)], compact aggregates of primary Carbopol particles are formed, separated from each other leading to a low elasticity value of the dispersion. In this regime, the material can be described as a dilute dispersion of hardly interacting agglomerates mixed presumably with individual primary particles, which are not detectable with our technique. In regime 2 [Fig. 9(a)(2)], increasing the  $pH$  induces a swelling of these aggregates and particles, which brings them closer to each other resulting in the formation of a closely packed structure described as a highly elastic sample spanning network with the maximum of elasticity. It has to be noted that the degree of swelling ( $SR > 2$ ) obtained at this polymer concentration of 0.5 wt. % is higher than that obtained at a low concentration of 0.01 wt. % ( $SR = 1.4$ ) as shown in Table I. This result can be explained by a higher ionic strength for a higher polymer concentration, which leads to an increase in osmotic pressure due to the presence of more ions and, consequently, to greater swelling capacities. In addition, despite the swelling of these agglomerates and individual particles, their core is still inaccessible for the tracer particles used here (200 nm), i.e., even at maximum bulk elasticity, the mesh size of the core of an individual particle is clearly below 200 nm.

Finally, increasing the  $pH$  even further [regime 3, Fig. 9(a)(3)] causes these structures to shrink because once the acid groups are fully dissociated, further addition of base

simply adds ions that screen the charges of the acid groups which reduces the electrostatic repulsions between them, decreases the osmotic pressure and this, in turn, reduces  $G_0$ , i.e., the structure softens.

*b. Polymer concentration effect.* Figure 8(b)(1) shows the variation of  $G_0$  as a function of polymer concentration for Carbopol Ultrez 10 solutions at three different concentrations, namely, 0.1, 0.2, and 0.5 wt. %. For each of the concentrations,  $G_0$  corresponds to the value of  $G_0$  at the maximum of elasticity upon variation of  $pH$ , i.e., at intermediate  $pH$  (regime 2). We observe a strong increase in the dispersion elasticity with increasing polymer concentration [39–42];  $G_0$  increases from 120 to 500 Pa for polymer concentrations ranging from 0.1 to 0.5 wt. %, respectively. To study corresponding changes in the Carbopol microstructure, MRM experiments were performed at these three different concentrations, and results are shown in Figs. 9(b)(1)–9(b)(3). Similar to the  $pH$  effect, evident microstructural changes are detected when increasing the polymer concentration. At the lowest concentration of 0.1 wt. % [Fig. 9(b)(1)], both viscous (blue) and elastic (red) accessible areas occupy  $29 \pm 3\%$  and  $13 \pm 6\%$ , respectively, and the inaccessible area (black)  $58 \pm 5\%$  of the total area. With increasing polymer concentration, we observe a decrease of both accessible viscous and elastic areas with at the same time a strong increase of the inaccessible ones (black) to reach  $87 \pm 3\%$  at 0.5 wt. % [Fig. 9(b)(4)]. However, with an inaccessible area fraction value of 58% at 0.1 wt. % and a fivefold increase in polymer concentration, the agglomerates and the highly crosslinked core of the primary particles should fill the entire space, but this is not the case. This result might be explained by shrinkage of the primary Carbopol particles at high concentrations due to a surplus of free ions outside of the particles, which reduces the osmotic pressure. Also, the average size of both accessible areas decreases with increasing polymer concentration as shown in Fig. S3(b) in the [supplementary material](#) [43].

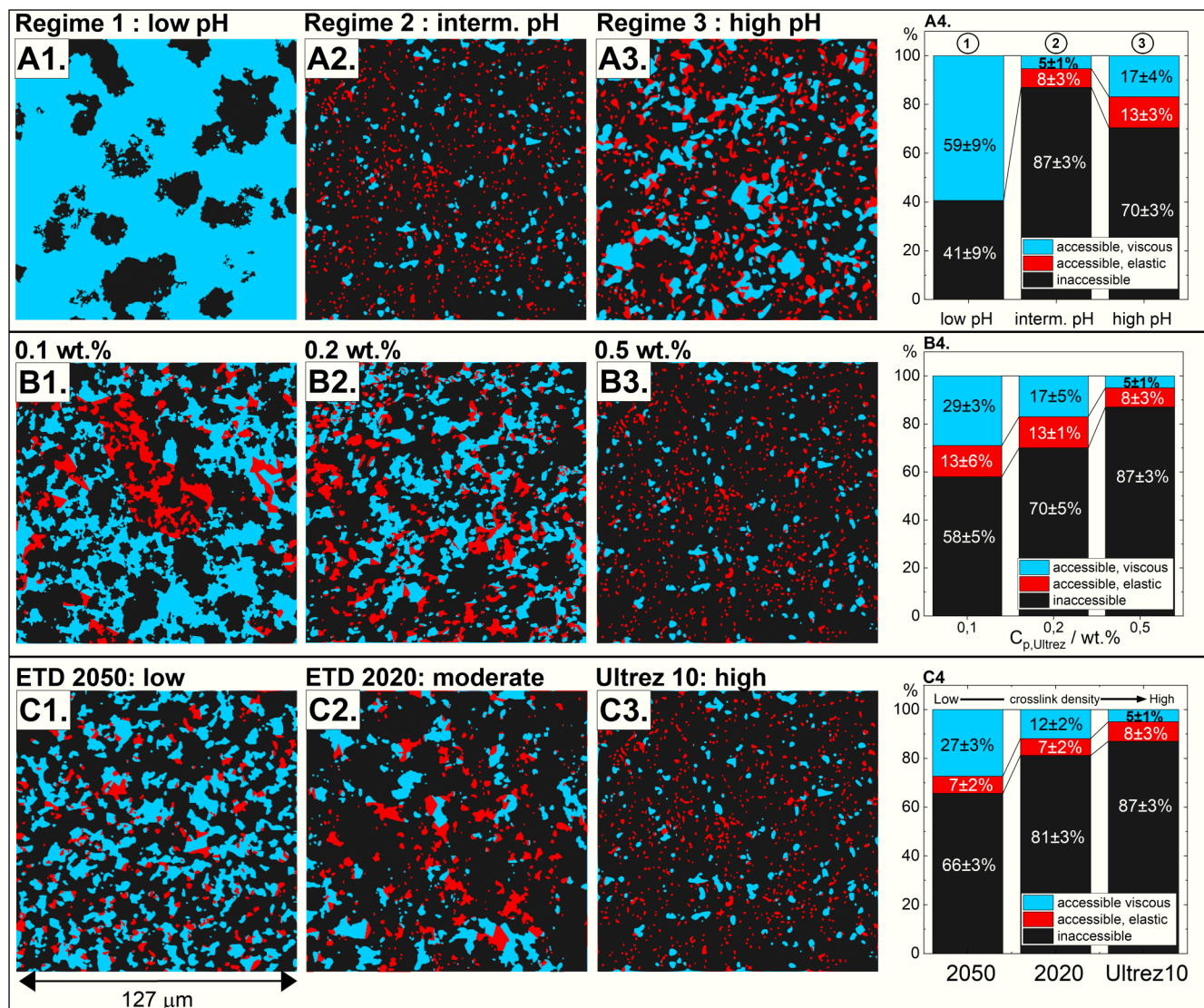


**FIG. 9.** Micro-rheo-mapping for *Upper row*: Ultrez 10 dispersions at a polymer concentration of 0.5 wt. % in the  $pH$  regimes indicated in Fig. 8(a)(1): low (a1), intermediate (a2), and high (a3). *Intermediate row*: Ultrez 10 at polymer concentrations  $C_{p,Ultrez}$  of 0.1 (b1), 0.2 (b2), and 0.5 (b3) wt. % corresponding to the  $pH$  of maximum elasticity. *Bottom row*: 0.5 wt. % Carbopol dispersions differing in their degree of crosslinking: ETD 2050 (c1), ETD 2020 (c2), and Ultrez 10 (c3) weakly, moderately, and highly crosslinked, respectively. Black areas correspond to a mixture of aggregates of primary Carbopol particles and individual primary particles inaccessible regions for the tracers. Blue and red areas to viscous and elastic accessible regions, respectively. (A4), (B4), and (C4) show the average fraction of the three areas by analyses of three different experiments for the respective sample series.

This result can be explained by an increasing overlap and compression of dangling ends or hairy surface layers leading to an increase in inaccessible areas at the expense of accessible and viscous regions.

*c. Crosslink density effect.* Finally, Fig. 8(c)(1) displays the variation of  $G_0$ , corresponding to the maximum elasticity, as a function of the degree of crosslinking of Carbopol. Clearly, the elasticity of the dispersion increases with the degree of crosslinking following the trend ETD 2050 < ETD 2020 < Ultrez 10.  $G_0$  increases from 40 to 350, to reach 500 Pa for 0.5 wt. % solutions of Carbopol ETD 2050, ETD 2020, and Ultrez 10, respectively. Results obtained from MRM measurements performed on these three samples are shown in Figs. 9(c)(1)–9(c)(3). Again, significant microstructural changes are observed when increasing the degree of crosslinking. The analysis of the distribution of the three

microscopic areas for each Carbopol [Fig. 9(c)(4)] shows that the increase in  $G_0$  is accompanied by a strong increase in the fraction of the inaccessible area (black) with increasing the degree of crosslinking. In particular, a significant gap is found between ETD 2050 with a fraction of 66 $\pm$ 3% and both ETD 2020 and Ultrez 10 with nearly similar fractions of 81 $\pm$ 3% and 87 $\pm$ 3%, respectively. At the same time, a decrease of both accessible elastic (red) and viscous (blue) areas is observed with also a continuous decrease of the average size of the viscous inclusions, while the size of the elastic area goes through a maximum with increasing degree of crosslinking [Fig. S3(c) in the supplementary material] [43].

These results may be explained by the significant differences in the structure of the agglomerates as observed at very low polymer concentrations in Sec. III B 1. We have shown that the average size, after neutralization, of an individual aggregate is much larger for both Carbopols ETD 2020 and

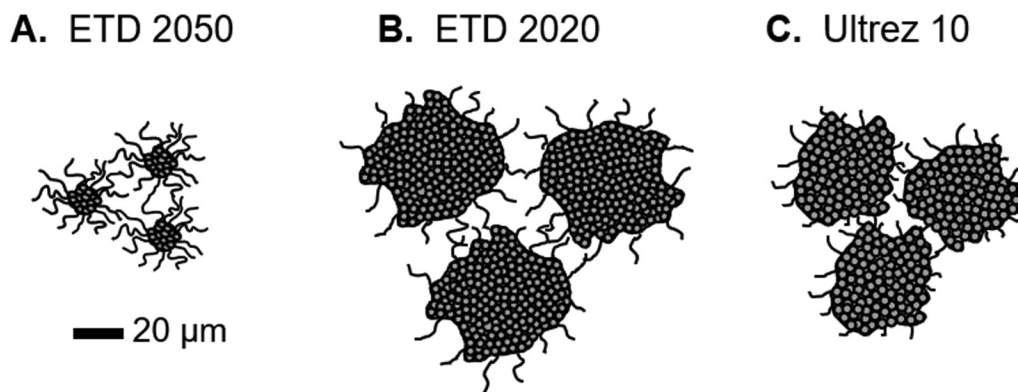


**FIG. 10.** Illustrations of the microstructure of 0.5 wt. % neutralized ETD 2050 (a), ETD 2020 (b), and Ultrez 10 (c) as deduced from MPT measurements.

Ultrez 10 with diameters of  $56 \pm 14$  and  $43 \pm 11$   $\mu\text{m}$ , respectively compared to the Carbopol ETD 2050 with a diameter of only  $10 \pm 2.5$   $\mu\text{m}$ . In addition, for ETD 2050, the number and length of polymer chains covering the core of one primary particle and thus the surface of the large aggregates are likely to be much greater than for the other two. A longer chain length in the shell surrounding the core in ETD 2050 prevents close contact between primary particles as well as between aggregates, therefore a smaller fraction of inaccessible area is observed, both at low and high polymer concentrations. The higher elasticity observed for Carbopol Ultrez 10, is likely due to an increase in the rigidity of the microstructure with closer contact between aggregates and/or primary particles due to a shorter dangling chain length but may also be due to a higher degree of crosslinking of the individual Carbopol particle.

In summary, from all these results an illustration of the microstructure of the three Carbopols at the maximum elasticity can be deduced as shown in Fig. 10.

## 2. Correlation between microstructure and macroelasticity

In order to establish a correlation between microstructure and macroelasticity, we investigated in more detail the

variations of two microscopic features likely to be related to the Carbopol macroelasticity, namely, the fraction of inaccessible area and the local apparent elastic modulus  $G_{0,MPT}$  and compared them to the variation of  $G_0$ . The variation of a third microscopic parameter, namely, the local apparent viscosity  $\eta_{MPT}$  was also determined (see Fig. S4 in the [supplementary material](#)) [43] but as this parameter is not suitable for describing material elasticity, it will not be discussed here. As defined previously, the inaccessible areas correspond to a mixture of aggregates of primary particles and individual primary particles formed of a highly crosslinked core and  $G_{0,MPT}$  to the local elasticity determined within the accessible elastic regions. Their variations as a function of  $pH$ , polymer concentration, and crosslink density are shown in the lower part of Fig. 8. In all cases, qualitatively, the variations of these two microscopic parameters follow the same trend as that of the macroscopic elastic modulus  $G_0$  [Figs. 8(a)(1)–8(a)(3)], which would indicate a direct correlation between microstructure and macroelasticity. For the  $pH$  effect, both parameters [Figs. 8(a)(2) and 8(a)(3)], as for  $G_0$ , go through a maximum upon increasing  $pH$ . For the effects of polymer concentration [Figs. 8(b)(2) and 8(b)(3)] and degree of crosslinking [Figs. 8(c)(2) and 8(c)(3)], the fraction of inaccessible areas as well as  $G_{0,MPT}$  continuously

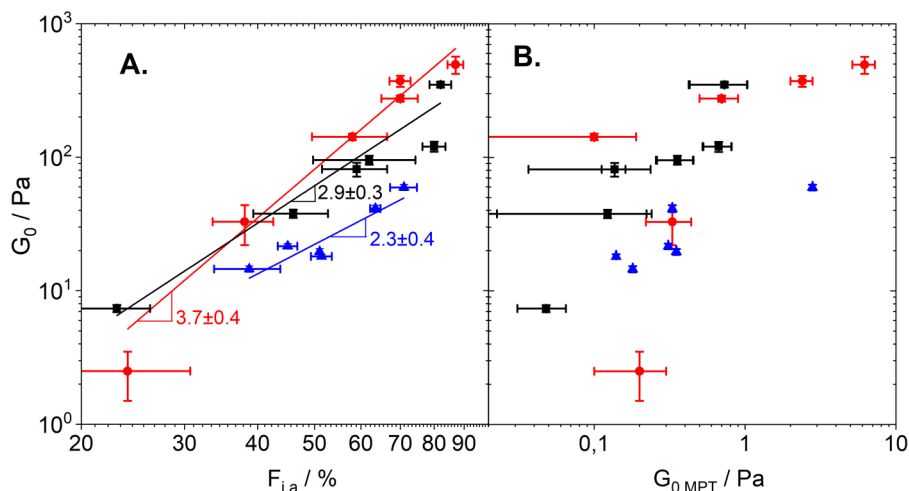


**FIG. 11.** Variations of the elastic plateau modulus  $G_0$  as a function of the fraction of the inaccessible area  $F_{i,a}$  (a) and as a function of the local apparent elastic modulus  $G_{0,MPT}$  for Ultrez 10 (red circles), ETD 2020 (black squares), and ETD 2050 (blue triangles) solutions.

increase, similar to  $G_0$ , with increasing polymer concentration and degree of crosslinking, respectively.

To quantify and compare the strength of the correlation between these two microscopic parameters and the bulk elasticity  $G_0$ , variations of  $G_0$  as a function of the fraction of inaccessible area and as a function of  $G_{0,MPT}$  are plotted in Figs. 11(a) and 11(b), respectively. Results are presented for neutralized solutions, at intermediate and high pH, for the three types of thickeners, namely, Ultrez 10 (red circles), ETD 2020 (black squares), and ETD 2050 (blue triangles) at polymer concentrations between 0.2 and 1 wt. %.

In a first approach, in Fig. 11(a), a power-law dependence of  $G_0$  on the fraction of inaccessible area is obtained for the three thickeners. From Fig. 11(b), although there seems to be a weak trend that  $G_0$  increases with increasing  $G_{0,MPT}$ , no clear correlation between  $G_0$  and  $G_{0,MPT}$  is visible. These results indicate that it is mainly the aggregates with their highly crosslinked cores that control the macroelastic properties of the thickeners.

In addition, as seen in Fig. 11(a), the scaling exponent decreases from  $3.7 \pm 0.4$  to  $2.9 \pm 0.3$  to reach  $2.3 \pm 0.4$  for Ultrez 10, ETD 2020, and ETD 2050, respectively, with lower absolute  $G_0$  values for ETD 2050. This result might be explained by differences in the degree of crosslinking between the thickeners, with the latter following the trend  $ETD\ 2050 < ETD\ 2020 < Ultrez\ 10$ .

#### IV. CONCLUSIONS

In this study, we used rotational rheometry as well as multiple particle tracking based microrheology to characterize macro- and microrheological properties of commercial acrylic thickeners of different degrees of crosslinking, namely, Carbopol Ultrez 10, ETD 2020, and ETD 2050, highly, moderately, and weakly crosslinked, respectively.

We developed a new microrheology method, namely, the so-called MRM technique, which allows us to obtain an accurate and direct visualization of the Carbopol microstructure. This new imaging technique combines the Voronoi triangulation technique results obtained from a conventional MPT microrheology analysis discarding short particle trajectories with the image overlay technique including all trajectories generated during a tracking experiment.

At low polymer concentration, i.e., in the diluted regime, we obtained structural information on agglomerates formed of primary Carbopol particles and estimated a diameter of  $43 \pm 11$ ,  $56 \pm 14$ , and  $10 \pm 2.5$   $\mu\text{m}$  for Carbopol Ultrez 10, ETD 2020, and ETD 2050, respectively. Results also suggest, in the case of ETD 2050, longer dangling chain ends surrounding these agglomerates as well as the core of the individual particles compared to the other two Carbopol grades.

At higher, technically relevant, polymer concentrations, results indicate that all three thickeners are highly heterogeneous on a micrometer length scale with a microstructure composed of several regions characterized by different crosslink densities. A first region inaccessible for tracer particles, which corresponds to a mixture of compact agglomerates of

primary Carbopol particles and individual primary particles with a very dense, highly crosslinked core of mesh size  $< 200$  nm and a second one, diluted enough to be accessible for the tracers, which comprises both elastic and viscous regions and for which we determined the local apparent elastic modulus  $G_{0,MPT}$  and viscosity  $\eta_{MPT}$ .

The study of the impact of pH, polymer concentration, and crosslink density on both microstructural and macrorheological properties of the three types of Carbopol allowed us to establish a correlation between microstructure and macroelasticity. In particular, we found that the bulk shear modulus  $G_0$  exhibits a power-law scaling with the fraction of inaccessible area, and exponents between 2.3 and 3.7 are found depending on the Carbopol grade. This strong correlation clearly shows that the agglomerates and the highly crosslinked core of the Carbopol control the bulk elasticity of the solutions. This new insight is based on the data obtained with our new MRM approach and would not have been accessible with conventional MPT experiments solely focusing on trajectories sufficiently long for reliable MSD calculation. Our results contribute to a better understanding of the thickening mechanism of Carbopols.

Finally, this new MRM visualization method could be used for future research, in particular, to explore and better understand the evolution of the microstructure in the aging and rejuvenation of Carbopol microgels. The method is also capable of revealing microstructural information about other heterogeneous fluids including viscous and elastic regions.

#### ACKNOWLEDGMENT

The authors would like to thank Lubrizol Advanced Materials for providing all Carbopol samples.

#### AUTHOR DECLARATIONS

##### Conflict of Interest

The authors have no conflicts to disclose.

#### REFERENCES

- [1] Jaworski, Z., T. Szychaj, A. Story, and G. Story, "Carbomer microgels as model yield-stress fluid," *Rev. Chem. Eng.* (2021) (published online).
- [2] Oppong, F. K., and J. R. de Bruyn, "Diffusion of microscopic tracer particles in a yield-stress fluid," *J. Non-Newtonian Fluid Mech.* **142**, 104–111 (2007).
- [3] Oppong, F. K., and J. R. de Bruyn, "Microrheology and jamming in a yield-stress fluid," *Rheol. Acta* **50**, 317–326 (2011).
- [4] Benmouffok-Benbelkacem, G., F. Caton, C. Baravian, and S. Skali-Lami, "Non-linear viscoelasticity and temporal behavior of typical yield stress fluids: Carbopol, xanthan and ketchup," *Rheol. Acta* **49**, 305–314 (2010).
- [5] Cloitre, M., and R. T. Bonnecaze, "A review on wall slip in high solid dispersions," *Rheol. Acta* **56**, 283–305 (2017).
- [6] Curran, S. J., R. E. Hayes, A. Afacan, M. C. Williams, and P. A. Tanguy, "Properties of carbopol solutions as models for yield-stress fluids," *J. Food Sci.* **67**, 176–180 (2002).
- [7] Ovarlez, G., S. Cohen-Addad, K. Krishan, J. Goyon, and P. Coussot, "On the existence of a simple yield stress fluid behavior," *J. Non-Newtonian Fluid Mech.* **193**, 68–79 (2013).

- [8] de Cagny, H., M. Fazilati, M. Habibi, M. M. Denn, and D. Bonn, "The yield normal stress," *J. Rheol.* **63**, 285–290 (2019).
- [9] Dinkgreve, M., M. Fazilati, M. M. Denn, and D. Bonn, "Carbopol: From a simple to a thixotropic yield stress," *J. Rheol.* **62**, 773–780 (2018).
- [10] de Souza Mendes, P. R., "Modeling the thixotropic behavior of structured fluids," *J. Non-Newtonian Fluid Mech.* **164**, 66–75 (2009).
- [11] Blackwell, B. C., and R. H. Ewoldt, "Non-integer asymptotic scaling of a thixotropic-viscoelastic model in large-amplitude oscillatory shear," *J. Non-Newtonian Fluid Mech.* **227**, 80–89 (2016).
- [12] Islam, M. T., N. Rodriguez-Hornedo, S. Ciotti, and C. Ackermann, "Rheological characterization of topical carbomer gels neutralized to different pH," *Pharm. Res.* **21**, 1192–1199 (2004).
- [13] Younes, E., M. Himl, Z. Stary, V. Bertola, and T. Burghelca, "On the elusive nature of Carbopol gels: 'model,' weakly thixotropic, or time-dependent viscoplastic materials?," *J. Non-Newtonian Fluid Mech.* **281**, 104315 (2020).
- [14] Graziano, R., V. Preziosi, D. Uva, G. Tomaiuolo, B. Mohebbi, J. Claussen, and S. Guido, "The microstructure of Carbopol in water under static and flow conditions and its effect on the yield stress," *J. Colloid Interface Sci.* **582**, 1067–1074 (2021).
- [15] Kowalczyk, A., C. Oelschlaeger, and N. Willenbacher, "Visualization of micro-scale inhomogeneities in acrylic thickener solutions: A multiple particle tracking study," *Polymer* **58**, 170–179 (2015).
- [16] Gutowski, I. A., D. Lee, J. R. de Bruyn, and B. J. Frisken, "Scaling and mesostructure of Carbopol dispersions," *Rheol. Acta* **51**, 441–450 (2012).
- [17] Géraud, B., L. Jørgensen, C. Ybert, H. Delanoë-Ayari, and C. Barentin, "Structural and cooperative length scales in polymer gels," *Eur. Phys. J. E* **40**, 5 (2017).
- [18] Lefrançois, P., E. Ibarboure, B. Payre, E. Gontier, J. F. Le Meins, and C. Schatz, "Insights into Carbopol gel formulations: Microscopy analysis of the microstructure and the influence of polyol additives," *J. Appl. Polym. Sci.* **132**, 42761 (2015).
- [19] Piau, J. M., "Carbopol gels: Elastoviscoplastic and slippery glasses made of individual swollen sponges meso- and macroscopic properties, constitutive equations and scaling laws," *J. Non-Newtonian Fluid Mech.* **144**, 1–29 (2007).
- [20] Shafiei, M., M. Balhoff, and N. W. Hayman, "Chemical and microstructural controls on viscoplasticity in Carbopol hydrogel," *Polymer* **139**, 44–51 (2018).
- [21] Lee, D., I. A. Gutowski, A. E. Bailey, L. Rubatat, J. R. de Bruyn, and B. J. Frisken, "Investigating the microstructure of a yield-stress fluid by light scattering," *Phys. Rev. E* **83**, 031401 (2011).
- [22] Baudonnet, L., D. Pere, P. Michaud, J. L. Grossiord, and F. Rodriguez, "Effect of dispersion stirring speed on the particle size distribution and rheological properties of carbomer dispersions and gels," *J. Dispersion Sci. Technol.* **23**, 499–510 (2002).
- [23] Baudonnet, L., J. L. Grossiord, and F. Rodriguez, "Effect of dispersion stirring speed on the particle size distribution and rheological properties of three carbomers," *J. Dispersion Sci. Technol.* **25**, 183–192 (2004).
- [24] Lochhead, R. Y., "The use of polymers in cosmetic products," in *Cosmetic Science and Technology*, edited by K. Sakamoto, R. Y. Lochhead, H. I. Maibach, and Y. Yamashita (Elsevier, New York, 2017), pp. 171–221.
- [25] Agarwal, M., and Y. M. Joshi, "Signatures of physical aging and thixotropy in aqueous dispersion of Carbopol," *Phys. Fluids* **31**, 063107-1–063107-11 (2019).
- [26] Lubrizol, Dispersion techniques for Carbopol polymers, TDS-103, Lubrizol, 2007.
- [27] Nesper, S., C. Bechinger, P. Leiderer, and T. Palberg, "Finite size effects on the close packing of hard spheres," *Phys. Rev. Lett.* **79**, 2348–2351 (1997).
- [28] Bubeck, R., C. Bechinger, S. Nesper, and P. Leiderer, "Melting and reentrant freezing of two-dimensional colloidal crystals in confined geometry," *Phys. Rev. Lett.* **82**, 3364–3367 (1999).
- [29] Crocker, J. C., and D. G. Grier, "Methods of digital video microscopy for colloidal studies," *J. Colloid Interface Sci.* **179**, 298–310 (1996).
- [30] Mason, T. G., K. Ganesan, J. H. van Zanten, D. Wirtz, and S. C. Kuo, "Particle tracking microrheology of complex fluids," *Phys. Rev. Lett.* **79**, 3282–3285 (1997).
- [31] Weeks, E. R., "Three-dimensional direct imaging of structural relaxation near the colloidal glass transition," *Science* **287**, 627–631 (2000).
- [32] Wirtz, D., "Particle-tracking microrheology of living cells: Principles and applications," *Annu. Rev. Fluid Mech.* **38**, 301–326 (2009).
- [33] Okabe, A., B. Boots, K. Sugihara, and S. N. Chiu, *Spatial Tessellations Concepts and Applications of Voronoi Diagrams*, 2nd ed. (Wiley, New York, 2000).
- [34] Lubrizol, Molecular weight of Carbopol® and Pemulen® polymers, TDS-222, Lubrizol, 2007.
- [35] Lubrizol, Polymers for pharmaceutical applications, Pharmaceutical Bulletin 1 (2020), pp 1–10.
- [36] Di Giuseppe, F., F. Corbi, A. Funicello, T. N. Massmeyer, M. Santimano, A. Rosenau, and A. Davaille, "Characterization of carbopol for experimental tectonics and geodynamics," *Tectonophysics* **642**, 29–45 (2015).
- [37] Davies, G. A., and J. R. Stokes, "Thin film and high shear rheology of multiphase complex fluids," *J. Non-Newtonian Fluid Mech.* **148**, 73–87 (2015).
- [38] Flory, P. J., *Principles of Polymer Chemistry* (Cornell University, Ithaca, N.Y., 1953).
- [39] Hassan, M. A., M. Pathak, and M. K. Khan, "Thermorheological characterization of elastoviscoplastic Carbopol Ultrez 20 gel," *J. Eng. Mater. Technol.* **137**(3), 031002 (2015).
- [40] Ketz, R. J., R. K. Prud'homme, and W. W. Graessley, "Rheology of concentrated microgel solutions," *Rheol. Acta* **27**, 531–539 (1988).
- [41] Bhattacharjee, T., C. P. Kabb, C. S. O'Bryan, J. M. Uruena, B. S. Sumerlin, W. G. Sawyer, and T. E. Angelini, "Polyelectrolyte scaling laws for microgel yielding near jamming," *Soft Matter* **14**, 1559–1570 (2018).
- [42] Lidon, P., L. Villa, and S. Manneville, "Power-law creep and residual stresses in a carbopol gel," *Rheol. Acta* **56**, 307–323 (2017).
- [43] See supplementary material at <https://www.scitation.org/doi/suppl/10.1122/8.0000452> for  $G_0$  (Fig. S1) and yield stress  $\tau_y$  (Fig. S2) values as a function of pH and polymer concentration for ETD 2050, ETD 2020, and Ultrez 10. For the variation of elastic and viscous area sizes as a function of pH [Fig. S3(a)], polymer concentration [Fig. S3(b)] for Ultrez 10 and as a function of the degree of crosslinking [Fig. S3(c)]. For local apparent viscosity  $\eta_{0,MPT}$  values as a function of pH [Fig. S4(a)(2)], polymer concentration [Fig. S4(b)(2)], and crosslink density [Fig. S4(c)(2)].